A NEW ENERGY-COMPATIBLE NONSTATIONARY STOCHASTIC GROUND-MOTION SIMULATION METHOD

Shaoqing Wang[1], Ruifang Yu[1*], Raffaele De Risi[2], Xiaojun Li[3,1]

[1]Department of Engineering Seismology, Institute of Geophysics, China Earthquake Administration, Beijing, China

[2]Department of Civil Engineering, University of Bristol, Bristol, UK

[3]College of Architecture and Civil Engineering, Beijing University of Technology, Beijng, China

A new time-frequency modulating function with a novel equivalent average-intensity envelope based on the instantaneous energy is proposed to simulate fully nonstationary ground motions. The new model utilizes simple, uncoupled, and statistically well-studied temporal and spectral nonstationary parameters. Then, a period-by-period simulation method based on the proposed stochastic model is developed to match multiple targets. A numerical comparison shows that the new method replicates well both the target temporal and spectral non-stationarities and it is efficient and easy to use in engineering practice. This study also demonstrates that for obtaining site-specific seismic input by means of site response analysis: (1) the frequency contents of bedrock motion, including the energy concentration in terms of frequency and frequency decaying with respect to time, have a significant impact on the site response with moderate and large PGA levels; (2) using the proposed instantaneous-frequency-related time modulating function to approximate the real ground motion leads to results sufficiently close to the record for nonlinear site response regardless PGA levels and site condition. Therefore, attention should be paid to the change of nonstationary characteristics of ground motion frequency according to the source, path and site condition when simulating ground motion on bedrock. As the proposed methods can approximately control various ground-motion characters, different targets of ground-motion simulation can be matched for different engineering purpose, such as site response analysis, time-history analysis of special structures, etc.

KEYWORDS

Ground-motion simulation; time-frequency modulating function; non-stationarity; spectral matching; nonlinear site response

1. Introduction

It is nowadays broadly accepted that the reliability of a seismic design depends on whether the input motion could accurately represent the expected seismic actions and their variability, regardless of how sophisticated the seismic design method is [Lee and Mosalam 2006; Cakir 2013]. However, accurate prediction of potential future ground motion is impossible due to the complexity of the focal mechanism, wave propagation, and site conditions. Consequently, it is necessary to study how to provide proper seismic input for structural design. To date, there are mainly two types of methods for seismic analysis of structures. The first is the response-spectrum analysis (RSA), which is widely recommended in several national building codes [CEN 2005; BSSC 2015; GB50011-2010 2016]. This method is specific for the analysis of linear systems, and it is suitable for classically or non-classically damped systems [Wilson et al. 1981; Zhou et al. 2004; Yu and Zhou 2007; Heredia-Zavoni 2011]. For the RSA, the input parameter is the design response spectra which can be obtained by seismic hazard assessment. However, for some critical structures (e.g. dams, bridges), the time-history analysis (THA) may be needed to perform nonlinear analyses to check the structural performance under large earthquakes. In this case, the input is, in general, acceleration time-histories. To get reasonable time-history, engineers can use selected natural records from strong-motion database based on the uniform hazard spectrum [Iervolino et al. 2010]. One may also resort to conditional mean spectrum to avoid large amplitudes at all spectral periods [Baker 2011]. However, due to the uneven distribution of earthquakes, suitable

* Corresponding author, Ph.D. Professor
Department of Engineering Seismology, Institute of Geophysics, China Earthquake Administration, Beijing, 100081, China
Address: No.5 Minzu Daxue Nanlu, Haidian District, Beijing, 100081, China.
Email: yrfang126@126.com

natural records for specific selection criteria may be sparse. Therefore, artificial motions are required as supplements [Iervolino et al. 2010].

At a specific site, reliable seismic input must take the site effects into accounts because they may increase the potential of seismic damage for some structures [Assimaki et al. 2012; Sextos et al. 2018]. This can be achieved by directly simulating ground motions using hazard spectrum with adjusted amplitude. However, De Risi et al. [2019] showed that a simplified method for site effects could be unreliable. Besides, for some region like China, the local ground-motion prediction equation (GMPE) only provide ground motion intensities on bedrock [Yu et al. 2013]. Therefore, one can obtain more rigorous site-specific seismic input by first simulating bedrock ground-motion and then performing site response analysis using the local geotechnical data.

The simulation of artificial motions inherently requires mimicking the temporal and spectral non-stationarities of natural ground motions for specific seismic source, path, and local site conditions [Radu and Grigoriu 2018]. This is because these features have a significant influence on both the nonlinear structural response [Kianoush and Ghaemmaghami 2011; Cakir 2013; Yazdani and Alembagheri 2017] and on the nonlinear site response [Assimaki et al. 2008; Assimaki and Li 2012; Régnier et al. 2016]. On one hand, the traditional time-modulating stochastic models took the temporal variation of motion into account [Amin and Ang 1968; Iyengar and Iyengar 1969]. On the other hand, the controlling of spectral non-stationarity suffers from the difficulty of extracting the law of time-varying frequency. In this regard, many fully nonstationary stochastic models have been proposed based on different methodologies [Conte and Peng 1997; Rezaeian and Der Kiureghian 2008; Cacciola 2010; Yamamoto and Baker 2013; Yang and Zhou 2015; Wang et al. 2018]. The synthesized time-histories are primarily required to match target response spectra [Lilhanand and Tseng 1987, 1988; Hancock et al. 2006; Al Atik and Abrahamson 2010; Huang and Wang 2017; Wang et al. 2019]. Meanwhile, different targets (e.g. strong-motion duration, peak ground motions, frequency content) are also decided according to the structural typology under scrutiny [Cacciola and Zentner 2012; Huang and Wang 2017; Wang et al. 2019].

Although there are many nonstationary models for describing ground motions, their use in engineering practice is still a niche. On one hand, to obtain reliable structural behavior under artificial seismic input (e.g., moving resonance, [Beck and Papadimitriou 1993]), stochastic ground-motion models should represent the features of real records. For single-degree-of-freedom systems, Iervolino et al. [2010] shows some artificial ground-motion models produce biased engineering demand parameters (EDPs); Tsioulou et al. [2018a, b] developed modification methods for a stochastic ground-motion model that can produce similar EDP distribution with that produced by records [Tsioulou et al. 2019]. While, for multiple-degree-of-freedom systems, stochastic models that can faithfully reproduce the hysteretic energy dissipated by structures compared with records are still unavailable [Colajanni et al. 2020]. Therefore, it is urgent to develop a stochastic model that can well control the non-stationary features of ground motion. On the other hand, it is also due to the complexity to obtain fully nonstationary stochastic models specifically suitable for engineering application. For example, several models of accelerograms based on evolutionary power spectrum density (EPSD) [Priestley 1987] have too many parameters to be defined/calibrated, or the modal parameters are not statistically analyzed for engineering application [Preumont 1985; Cacciola 2010; Yamamoto and Baker 2013]. For example, using wavelet transform [Iyama and Kuwamura 1999; Spanos and Failla 2004] to estimate the parameters, Wang et al. [2018] obtained a series of time-dependent envelope functions for different frequencies. It is perfect for reconstructing real ground motions but hard to use in engineering practice. Therefore, Yu et al. [2015] constructed a fully nonstationary model trying to simplify the construction of EPSD representing (a) the temporal non-stationarity with one single time-modulating function and (b) the spectral non-stationarity with instantaneous/predominant frequency (F_p), separately. Such a method is particularly suitable for engineering practice for its fewer parameter numbers and well-studied parameters. However, the temporal non-stationarity is not emphasized and checked in Yu et al. [2015]; in this study it is demonstrated that to overcome the previous shortcomings and to avoid biased prediction of the energy accumulation, it is possible to use proper time-modulating functions. Therefore, the first objective of this study is to define an improved model based on Yu et al. [2015] with the ability to statistically predict the energy build-up and instantaneous frequency simultaneously. The second objective is to propose a method using the new model for simulating spectrum-compatible ground motions with both temporal and spectral non-stationarities for engineering practice. Moreover, the ground-motion simulation method proposed herein will help discussing considering also site-specific seismic input through site response analysis.

The paper is organized as follow. First, a new time-frequency modulating function for synthesizing fully nonstationary ground motion with desired non-stationarities is developed for engineering purpose. A new concept, named equivalent

average intensity-modulating function of EPSD, is proposed to directly use the intensity envelope of the accelerogram without separating it into narrow frequency bands. Then, a period-by-period method is discussed to adjust the synthesized initial ground motion matching both the target response spectrum and instantaneous frequency. Next, a case study is presented to show the improvement of the new method. Finally, sensitivity analysis is performed to show the influence on site response of core factors of bedrock-motion simulation, including frequency contents and non-stationarity and selection of time-frequency modulating function. Based on each result, instructions on how to include non-stationarities of bedrock motion into obtaining site-specific seismic input are proposed. The entire work, including a new fully nonstationary model, a ground-motion simulation method, and instructions on parameter settings, produces a practical framework to obtain reliable site-specific seismic input.

2. New time-frequency modulating functions for engineering application

2.1 Stochastic ground-motion model

The time-frequency modulating function proposed in Yu et al. [2015] to synthesize ground motion is based on the concept of EPSD [Priestley 1987] and the following stochastic model [Nigam and Mark 1984]:

$$y(t) = \int_{-\infty}^{+\infty} B(t,\omega) e^{i\omega t} \mathrm{d}F(\omega) \tag{1}$$

where $i = \sqrt{-1}$, ω is the circular frequency, $B(t,\omega)$ is the deterministic time-frequency modulating function, reflecting the time-frequency amplitude of the time-history, and $\mathrm{d}F(\omega)$ is an mutually-independent, zero-mean, and orthogonal increment process having the following properties:

$$\mathrm{E}[\mathrm{d}F(\omega)] = 0 \tag{2a}$$

$$\mathrm{E}[|\mathrm{d}F(\omega)|^2] = S(\omega)\mathrm{d}\omega \tag{2b}$$

where $\mathrm{E}[\cdot]$ denotes the expected value operator and $S(\omega)$ is the spectral density function, which can be obtained through the empirical relationship with the response spectral acceleration [Kaul 1978]. The EPSD is:

$$S(t,\omega) = |B(t,\omega)|^2 S(\omega). \tag{3}$$

Adopting the equation proposed by Shinozuka and Jan [1972], Equation (1) can be rewritten as the superposition of harmonics with random phases:

$$\begin{aligned} y(t) &= \sqrt{2}\sum_{k=1}^{n} [2S(t,\omega_k)\cdot\omega_k]^{1/2} \cos(\omega_k t + \phi_k) \\ &= \sum_{k=1}^{n} 2B(t,\omega_k)\sqrt{S(\omega_k)\Delta\omega}\cos(\omega_k t + \phi_k) \end{aligned} \tag{4}$$

where $\Delta\omega = \omega_{k+1} - \omega_k$, and ϕ_k is a uniform random phase distributed within $[-2\pi, 2\pi]$.

2.2 Time-frequency modulating functions

Above mentioned $B(t,\omega)$ is not unique according to different estimation techniques, including the temporal nonstationary-only models and fully nonstationary models. If only considering the temporal variation of ground motion, the modulating function $A(t)$ [Amin and Ang 1968; Iyengar and Iyengar 1969] can be seen as a simplification of $B(t,\omega)$. FIGURE 1 gives an example of accelerogram with its corresponding $A(t)$, which is the root-square of normalized moving average of the squared acceleration. A 3-second window for averaging is used to satisfy the "slowly" varying assumption of modulation function [Conte and Peng 1997]. In this case, Equation (4) can be simplified as:

$$y(t) = A(t)\sum_{k=1}^{n} 2\sqrt{S(\omega_k)\Delta\omega}\cos(\omega_k t + \phi_k) \tag{5}$$

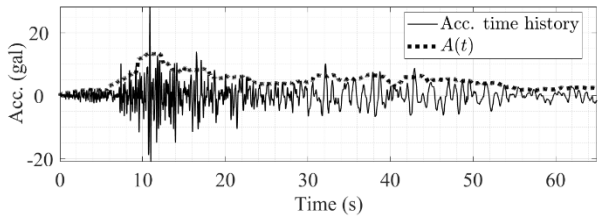

FIGURE 1 An example of accelerogram and intensity-modulating function

However, it is necessary to introduce in the frequency non-stationarities because $A(t)$ cannot reflect the frequency variation. In Yu et al. [2015], $B(t,\omega)$ is a simple combination of the frequency-independent intensity model $A(t)$ and an instantaneous-frequency-related model $L(t,f)$. The latter is:

$$L(t,f) = \frac{f}{F_p(t)} \exp\left(-\frac{f-F_p(t)}{F_p(t)}\right) \tag{6}$$

in which f is the frequency and $F_p(t)$ is the instantaneous frequency estimated via continuous Morlet wavelet transform using the method in Todorovska [2001]. The model of $F_p(t)$ is well established for ground motions grouped by magnitude, distance, direction, and site, which can approximately predict the variation of frequency of future ground motion.

If adopting the intensity envelope $A(t)$, the time-frequency distribution of ground motion is

$$WB(t,f) = A^2(t)L(t,f) \tag{7}$$

The time-frequency modulating function $B(t,\omega_k)$ with discrete circular frequency ω_k thus can be obtained by normalizing Equation (7), that is:

$$B(t,\omega_k) = \frac{WB(t,\omega_k)}{\max[WB(t,\omega_k)]} \tag{8}$$

FIGURE 2b shows examples of Equation (8) with its corresponding $F_p(t)$ in FIGURE 2a. The model gives a good prediction of frequency variation as $B(t,\omega_k)$ emphasizes the frequency contents near F_p. However, as shown in the following, it struggles at predicting the instantaneous energy of the ground motion.

As the target intensity envelope is $A(t)$, the energy build-up is regulated by $A^2(t)$ according to Parseval theorem [Kelkar et al. 1983]. Meanwhile, the instantaneous energy can also be approximately measured by the variance of the signal $\mathrm{Var}[y(t)]$, that can be calculated adopting Equation (8):

$$\mathrm{Var}[y(t)] = \int_{-\infty}^{+\infty} B^2(t,\omega)S(t,\omega)\mathrm{d}\omega = \int_{-\infty}^{+\infty} \frac{A^4(t)L^2(t,\omega)}{\max[A^4(t)L^2(t,\omega)]} S(t,\omega)\mathrm{d}\omega \tag{9}$$

FIGURE 2c plots the comparison between the target energy build-up $A^2(t)$ (grey dashed line) and the normalized $\mathrm{Var}[y(t)]$ using $B(t,\omega)$ (black solid line). It can be seen this model cannot fit the target energy build-up, especially within the time interval with lower instantaneous frequency.

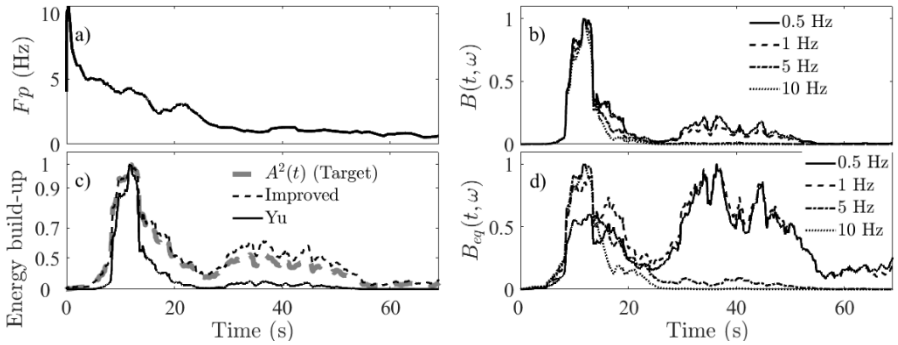

FIGURE 2 (a) Target $F_p(t)$. (b) Example of $B(t,\omega)$ in Yu model for different frequencies. (c) Comparison of energy build-up between the target and the synthesized ground motion using $B(t,\omega)$ (black solid line) and $B_{eq}(t,\omega)$ (black dashed line, see Section 2.3). (d) Example of $B_{eq}(t,\omega)$ using the improved model (see Section 2.3)

2.3 Improved $B_{eq}(t,\omega)$ based on instantaneous energy

As the model in Yu et al. [2015] has a biased energy build-up, it is necessary to revise it. The key point for revising is assuming that the normalized F_p-related $WB(t,f)$ should provide approximation for the shape of the energy distribution of the ground motion. Therefore, the energy build-up can be matched through reformulating $WB(t,f)$.

Assume a family of temporal envelope functions $A_f(t,f)$ as intensity-modulating functions corresponding to different f. Replacing $A(t)$ in Equation (7) with $A_f(t,f)$, the normalized wavelet spectrum model will be

$$WB_f(t,f) = {A_f}^2(t,f)L(t,f) \tag{10}$$

According to Iyama and Kuwamura [1999], the relationship between the wavelet coefficient $\alpha_{j,k}$ and the energy distribution of the ground motion $En_{j,k}$ during the time interval $[t_{j,k}\Delta t - 2^j\Delta t, t_{j,k}\Delta t + 2^j\Delta t]$ at scale 2^j of discrete wavelet transform is

$$En_{j,k} = 2^{-j}\Delta t^2\alpha_{j,k}^2 \qquad 1 \le j \le \log_2 N - 2 \tag{11}$$

where Δt is the time step and N is the length of the signal; j and k are integrals respectively referring frequency level and time index; and 2^j is the scale of the wavelet:

$$2^j = \frac{f_s}{f_{cw}} \tag{12}$$

where f_s is the sampling frequency of ground motion, and f_{cw} is the central frequency of the wavelet at scale 2^j.

As we apply continuous wavelet transform to estimate $L(t,f)$, the shape of the energy distribution in Equation (11) is adopted as only an approximation, and the scale 2^j becomes $2^{j/\nu}$, in which $\nu = 10$ is usually referred to as the number of voices per octave. Moreover, as the frequency of the wavelet transform is discrete, we assume the energy within the frequency window around the scale $2^{j/\nu}$ is uniform:

$$En(t,f) = \frac{f_{cw}\Delta t^2\alpha_{j,k}^2}{f_{width}} \qquad \frac{3f_s}{2^{(j+2)/\nu}} \le f \le \frac{3f_s}{2^{(j+1)/\nu}}, \tag{13}$$

where $En(t,f)$ is the approximate energy distribution of the accelerogram; $f_{width} = 3f_s/2^{(j+2)/\nu}$ is the frequency window width, and $f_{cw} = f_s/2^{j/\nu}$ within the frequency window $[\frac{3f_s}{2^{(j+2)/\nu}}, \frac{3f_s}{2^{(j+1)/\nu}}]$.

Then, assuming the shape of $\alpha_{j,k}$ is same with $WB_f(t,f)$ in Equation (10), the normalized energy distribution or normalized ESPD S_E can be approximately calculated as follows:

$$S_E \approx \frac{f_{cw}A_f^4(t,f)L^2(t,f)}{f_s f_{width} C_s} \tag{14}$$

where $C_s = \max\left[\frac{f_{cw}A_f^4(t,f)L^2(t,f)}{f_s f_{width}}\right]$ is the normalization factor.
Defining the maximum of EPSD as M_E, the EPSD is

$$\hat{S}(t,f) \approx S_E \cdot M_E = \frac{f_{cw}A_f^4(t,f)L^2(t,f)}{f_s f_{width} C_S} \cdot M_E \tag{15}$$

Thus, the total instantaneous energy of the ground motion can be approximately measured by $\mathrm{Var}[y(t)]$, i.e.,

$$\mathrm{Var}[y(t)] \approx \int_{-\infty}^{+\infty} \hat{S}(t,f)\mathrm{d}\omega = \int_{-\infty}^{+\infty} \frac{f_{cw}A_f^4(t,f)L^2(t,f)}{f_s f_{width}} M_E \mathrm{d}\omega \tag{16}$$

In Equations (15) and (16), the term $A_f(t,f)$ represents a series of functions related to frequency, which are hard to determine. Thus, a single equivalent average intensity-modulating function $A_{eq}(t)$ is proposed to replace $A_f(t,f)$, which maintains the instantaneous energy same with using the family $A_f(t,f)$:

$$\mathrm{Var}[y(t)] \approx \int_{-\infty}^{+\infty} \frac{f_{cw}{A_f}^4(t,f)L^2(t,f)}{f_s f_{width}} M_E \mathrm{d}\omega = A_{eq}^4(t) \int_{-\infty}^{+\infty} \frac{f_{cw}L^2(t,f)}{f_s f_{width}} M_E \mathrm{d}\omega \tag{17}$$

As mentioned before, $A^2(t)$ regulates the energy build-up of the ground motion:

$$A^2(t) = \frac{\mathrm{Var}[y(t)]}{\max[\mathrm{Var}[y(t)]]} \tag{18}$$

Combined with Equation (17), as f_s, M_E, and $\max[\mathrm{Var}[y(t)]]$ are all constants, it is possible to obtain:

$$A_{eq}(t) = \left(\frac{A^2(t)}{\int_{-\infty}^{+\infty} f_{cw}L^2(t,f)\mathrm{d}\omega / f_{width}}\right)^{\frac{1}{4}} \cdot \frac{1}{C_E} \tag{19}$$

where $C_E = \max\left[\left(\frac{A^2(t)}{\int_{-\infty}^{+\infty}\int_{-\infty}^{+\infty} f_{cw}L^2(t,f)\mathrm{d}\omega / f_{width}}\right)^{\frac{1}{4}}\right]$. Replacing $A_f(t,f)$ in Equation (15) with $A_{eq}(t)$, it is possible to derive:

$$\hat{S}(t,f) \approx \frac{f_{cw}{A_{eq}}^4(t)L^2(t,f)}{C_S} \cdot M_E \tag{20}$$

Combining Equation (20) and Equation (3), as $S(\omega)$ and f_{cw} are time-independent, the normalized time-dependent modulating function $B_{eq}(t,\omega_k)$ at ω_k with compatible instantaneous energy becomes

$$B_{eq}(t,\omega_k) = \sqrt{\frac{\hat{S}(t,\omega_k)}{\max[\hat{S}(t,\omega_k)]}} = \frac{A_{eq}^2(t)L(t,\omega_k)}{\max[A_{eq}^2(t)L(t,\omega_k)]} \tag{21}$$

A comparison between $A_{eq}(t)$ and $A(t)$ is plotted in FIGURE 3. FIGURE 2d plots examples of revised $B_{eq}(t,\omega)$ having the same target $A(t)$ and $F_p(t)$ models with FIGURE 2b. Here, the form of $A_{eq}(t)$ is same with $A(t)$, that is, a single envelope function. Moreover, FIGURE 2c also shows the comparison between target energy build-up $A^2(t)$ and $\mathrm{Var}[y(t)]$ using $B_{eq}(t,\omega)$, shown as the black dash line, which is much closer to the target than that using $B(t,\omega)$, indicating a better prediction of energy build-up regulated with $A(t)$ than using $B(t,\omega)$ in Yu et al. [2015].

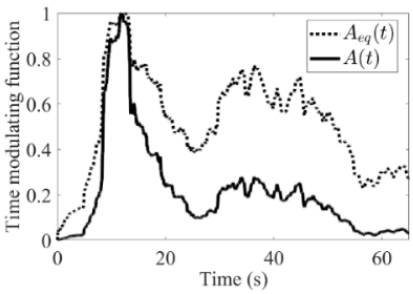

FIGURE 3 Intensity-modulating function (solid line) and equivalent average intensity-modulating function (dashed line)

3. Fully nonstationary spectrum-compatible accelerogram simulation method

Once the initial motion is constructed by Equation (1), iterative adjustment is required to match the target spectral acceleration (SA) and peak ground acceleration (PGA) according to design provisions. In this method, extra targets including $F_p(t)$ and energy build-up should also be examined and fitted to obtain desired non-stationarities. The energy build-up has been corrected to fit the target in the phase of synthesizing initial motion. While $F_p(t)$ must be corrected during the iterative adjustment. Because except for $B(t,\omega)$ that emphasizes the near-F_p contents, the empirical power spectrum $S(\omega)$ also determines the time-frequency distribution, making F_p concentrates near the peak value of $S(\omega)$. In this section, a method for matching the response spectrum is presented and a framework with some detail is also discussed to show how to simulate spectrum-compatible ground motion matching target temporal and spectral non-stationarities.

3.1 Iterative adjustment to fit spectrum and instantaneous frequency

A well-known wavelet method proposed by Lilhanand and Tseng [1987, 1988] is modified with the proposed time-frequency modulating function $B_{eq}(t,\omega)$ to match the target spectrum because it can maintain the main feature of the initial motion [Hancock et al. 2006; Giaralis and Spanos 2009; Al Atik and Abrahamson 2010; Wang et al. 2019]. The Lilhanand and Tseng method assumes that the time of peak response does not change before and after the adjustment of the accelerogram. This assumption is, however, not always valid for all controlling periods, especially for those very close to each other, which causes divergence in simulation. In our method, as we modify the adjustment time-history by multiplying $B_{eq}(t,\omega)$, which is non-analytical, to maintain the spectral non-stationarities, we use other than the matrix solution but a period-by-period method to determine the adjustment coefficient. The new method sacrifices some of the numerical speed but obtains excellent numerical stability.

Assuming there are N periods required to match the target spectrum, sequenced in descending order as $T_1, T_2, \ldots T_i, \ldots T_N$, the adjustment of SA period by period from the first to the last is defined as a Loop.

Supposing the accelerogram before fitting the ith period is $y^{i-1}(t)$, the misfit of spectral acceleration between the current spectrum $\mathrm{SA_C}(T_i)$ and target spectrum $\mathrm{SA_T}(T_i)$ with the ith period is

$$\Delta\mathrm{SA}(T_i) = \mathrm{SA_T}(T_i) - \mathrm{SA_C}(T_i) \tag{22}$$

Then, $\Delta\mathrm{SA}(T_i)$ should equal to the response acceleration of the adjustment time-history at t_m, which is the time of

the peak response of $y^{i-1}(t)$, that is,

$$\Delta \mathrm{SA}(T_i) = \int_0^{t_m} \delta y^i(t) h(t_m - t) \mathrm{d}t \tag{23}$$

where $\delta y^i(t)$ is the adjustment acceleration of the ith period, which can be obtained by multiplying a unit adjustment function with a scaling factor r, that is,

$$\delta y^i(t) = r \cdot B_{eq}(t, \omega_i) h(t_m - t) \tag{24}$$

In the above formula, $\omega_i = 2\pi/T_i$, and $B_{eq}(t, \omega_i)$ is the time-modulating function to maintain the time-varying frequency of the initial motions with ω_i, which can also be $B(t, \omega_i)$ from Yu et al. [2015] or the temporal intensity envelope $A(t)$ in Section 2.2 adopting different methods. $h(t_m - t)$ is selected to form the unit adjustment acceleration for it is the acceleration impulse response of damped single-degree-of-freedom system, that is,

$$h(t_m - t) = \exp\big(\xi \omega_i (t - t_m)\big) \cos[\omega_{Di}(t_m - t) + \varphi_i] \tag{25}$$

where ξ is the damping ratio; $\omega_{Di} = \omega_i \sqrt{1 - \xi^2}$ is the free-vibration frequency of the damped system; and φ_i is the initial phase of $h(t_m - t)$.

Combing Equations (23)-(25), we can obtain that

$$\Delta \mathrm{SA}(T_i) = C \cdot r \tag{26}$$

in which C is essentially the response acceleration of the unit adjustment function at t_m:

$$C = \int_0^{t_m} B_{eq}(t, \omega_i) h^2(t_m - t) \mathrm{d}t \tag{27}$$

Once C is calculated, r can be obtained from Equation (26) and then $\delta y^i(t)$ from Equation (24). Next, the acceleration after fitting the ith period is

$$y^i(t) = y^{i-1}(t) + \delta y^i(t) \tag{28}$$

Then, using $y^i(t)$ as the acceleration before fitting the $(i+1)$th period and repeating Equations (22)-(28), we can obtain $y^{i+1}(t)$ until one Loop for all periods is finished. Next, we iterate the Loops until the largest misfit is less than the tolerance. As the non-smoothed $F_p(t)$ and envelope function $B_{eq}(t, \omega_i)$ corrupt the displacement and velocity time-histories with baseline drift, a baseline-correction procedure based on polynomial fitting is also performed after every Loop.

3.2 Framework to fit SA and F_p

A flowchart illustrating the detailed procedure presented as following is plotted in FIGURE 4.

Given the target response spectral acceleration $\mathrm{SA_T}$ (red dots in FIGURE 5a), target PGA, and target F_p (dash line in FIGURE 6d), and the $\mathrm{SA_T}$ sorted by descend $T_1, T_2, \ldots, T_N$, we perform the following steps to fit SA and F_p.

1) Calculate $\mathrm{SA_C}(T_1)$ of the initial motion $y^0(t)$ and compare it with the target $\mathrm{SA_T}(T_1)$. If the misfit is larger than the tolerance, e.g. 5 percent, adjust the accelerogram using Equations (22)-(28) to obtain $y^1(t)$. Then finish one Loop by repeating this step from T_2 to T_N.

FIGURE 5 shows an example matching the 14th period ($T_{14} = 1.7$ s) from $y^{13}(t)$. As FIGURE 5a shows, the

discrepancy between $\mathrm{SA_T}(T_{14})$ and $\mathrm{SA_C}(T_{14})$ is $\Delta\mathrm{SA}(T_{14}) = 10.79$ gal. To eliminate it, a unit adjustment acceleration is created by Equation (25) multiplying with $B_{eq}(t, \omega_{14})$, shown as the solid line in FIGURE 5d, of which the response at the time of peak response of $y^{14}(t)$ is $C = 4.23$ gal. Thus, the adjustment scaling coefficient is $r = 2.55$ by Equation (26), as shown in FIGURE 5e. Multiplying r with the unit adjustment acceleration, we can obtain $\delta y^{14}(t)$ (the dash line in FIGURE 5d). Finally, by adding $y^{13}(t)$ to $\delta y^{14}(t)$, we get $y^{14}(t)$ (FIGURE 5f) and the spectral acceleration with $T_{14} = 1.7$ s matches the target (solid line in FIGURE 5a and black dot in FIGURE 5h).

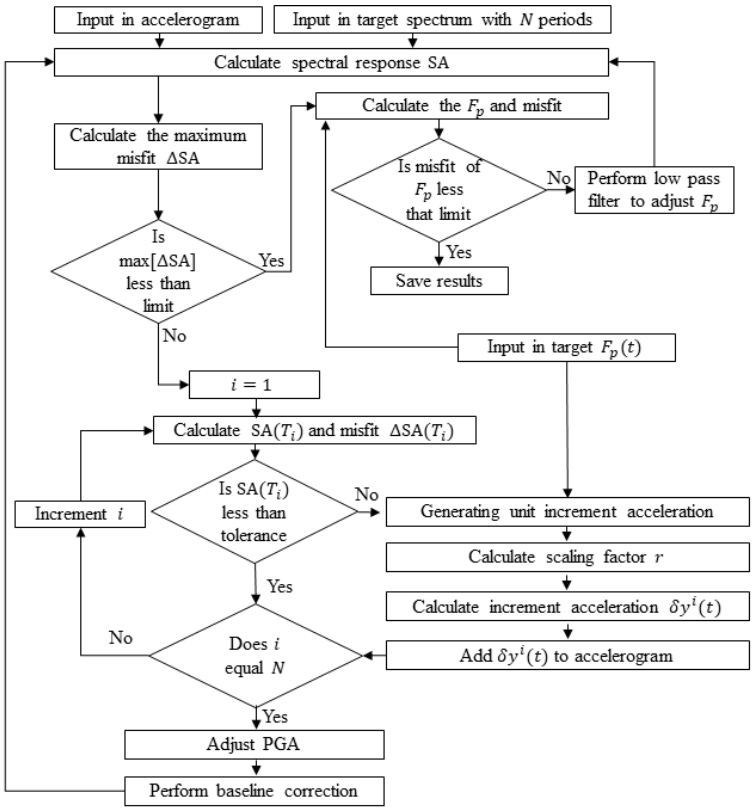

FIGURE 4 Detailed procedure to match SA and F_p.

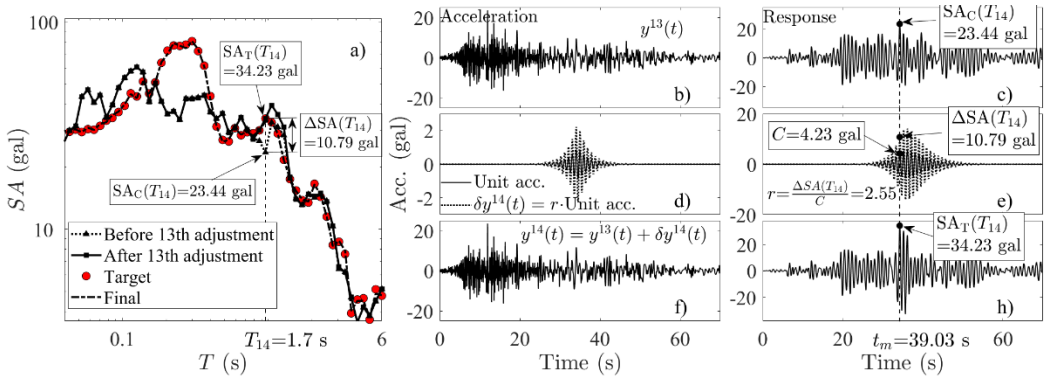

FIGURE 5 Example for matching spectrum: adjusting the 14th period ($T_{14} = 1.7$ s) of the first Loop.

2) Replace the PGA of the modified motion with the target PGA and perform baseline correction.

3) Repeat step 1) and step 2) until all the modified SA with $T_1, T_2, \ldots, T_N$ and the PGA both meet the requirements.

4) Calculate the instantaneous frequency of the accelerogram. Within those time intervals that the current F_p is too

higher than the target, perform a low-pass average filter with the width of the time window equaling three times the mean F_p in that time interval.

5) Repeat steps 1)-4) until the SA and F_p both meet the requirements.

FIGURE 6 illustrates the resulting time-histories after the adjustment procedure compared with the initial motion (after baseline correction). The modified spectrum is plotted as the triangle-dash line in FIGURE 5a. It can be seen that the adjustment procedure well maintains the main character of all the initial acceleration, velocity, and displacement. Moreover, the discrepancy of the F_p between the initial and target is reduced.

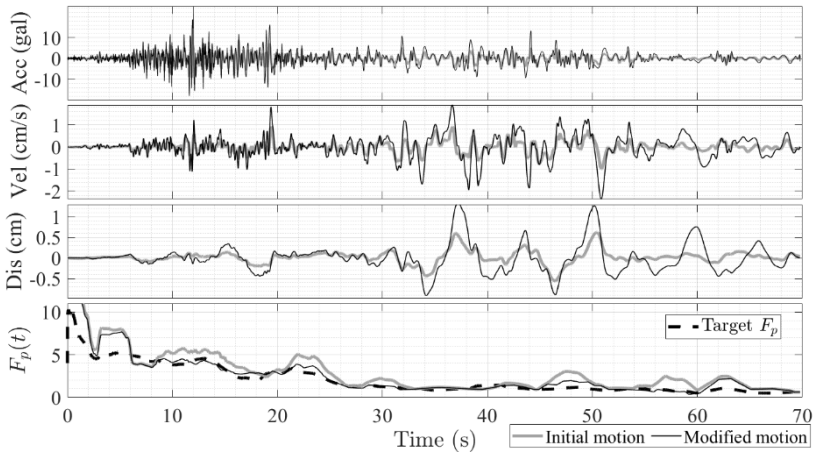

FIGURE 6 Acceleration, velocity, displacement and $F_p(t)$ after the procedure for matching both target SA and F_p, compared with the initial motion (after baseline correction)

4. Simulation of nonstationary ground motions based on different time-frequency modulating functions

To show the effects of different time-frequency modulating function on ground-motion simulation, three time-modulating functions described in Section 2 are chosen to simulate ground motions. The frequency-independent $A(t)$ is referred as 'Temporal'; the function $B(t,\omega)$ from Yu et al. [2015] presented in Section 2.2 is named 'Yu' and the proposed one $B_{eq}(t,\omega)$ in Section 2.3 is referred as 'Improved'.

4.1 Simulation scenarios and targets

In this section, the simulation targets are extracted from a real record for simplification. If using for engineering practice, the targets from codes and statistical research are preferred. As the 'Yu' and 'Improved' models are based on the wavelet-related model in Equation (6), the similarities of the models and the wavelet spectra of 20 ground motions from NGA PEER database [Chiou et al. 2008] are first investigated. Meanwhile, it is better that the record motion shows clear spectral variation that the replication of spectral non-stationarity using the new method can be compared. Therefore, we choose the NS component recorded at UP90S-H1 of 1990 Upland earthquake to extract the targets, as shown in FIGURE 7, for the similarity of its wavelet spectrum with the model of Equation (6) (FIGURE 7c) and the decaying of high frequency content towards end of the time (FIGURE 7d).

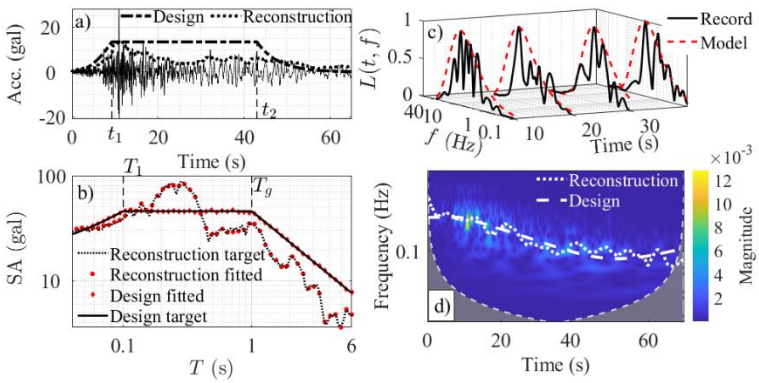

FIGURE 7 NS component recorded at UP90S-H1 of 1990 Upland earthquake and extracted simulation targets. (a) Acceleration time-history of record and target intensity envelopes. (b) Target and fitted spectral accelerations. (c) Examples of normalized frequency-dependent wavelet spectrum at time=10, 20, 30, 40 seconds and the models established in Equation (6). (d) Wavelet spectrum of the record and extracted target instantaneous frequencies.

Two different scenarios, named 'Reconstruction' and 'Design', are presented in this section to compare the behavior of three modulating functions for reconstructing a real record and for design purpose, respectively. Therefore, two intensity-envelope models, two $F_p(t)$ models, and two response spectra are extracted from the record and adopted for the two scenarios, which are also illustrated in FIGURE 7 and described as following:

Reconstruction scenario: The models are directly fitted from the record to reflect the fine variation of intensity and frequency contents. The intensity envelope is the root-square of normalized moving average of the squared recorded acceleration with a 3-second window (dot line in FIGURE 7a); the F_p model is estimated from the real acceleration by using continuous Morlet wavelet transformation (dot line in FIGURE 7d); and the target spectrum is directly calculated from the record (black dot line in FIGURE 7b).

Design scenario: The models adopt design forms from statistical studies. For simplification, the modal parameters are obtained by fitting the time-histories to those design forms rather than directly from those statistical studies, because there is no specific site for choosing proper parameters. The intensity model is from Amin and Ang [1968], as the dot-dash line shows in FIGURE 7a where $t_1 = 9.23$ s and $t_2 = 43.00$ s are respectively the time of 5% and 85% Arias intensity, and $c = 0.128$; The $F_p(t)$ model [Yu et al. 2015] is

$$F_p(t) = f_0 + p\exp(-st)\sin(\omega_f t) \tag{29}$$

where $f_0 = 6$ Hz, $p = 15$, $s = 0$, and $\omega_f = -0.02$ are modal parameters obtained by least-square method fitting the instantaneous frequency (dash line in FIGURE 7d); and the target spectrum uses a form of normalized design spectrum [Chopra 2012] close to the record spectrum shown as the black solid line in FIGURE 7b where $T_1 = 0.1$ s and $T_g = 1$ s.

Table 1 illustrates the required temporal and spectral nonstationary models and equations for simulating ground motions using 'Temporal', 'Yu', and 'Improved' methods. In each scenario and using each method, we simulate seven uncorrelated accelerograms by first synthesizing initial motions using Equation (4) or (5) and then adjusting them to match the target SA (and target F_p for 'Yu' and 'Improved') using the framework in Section 3.2. 81 controlling periods from 0.04 s to 6 s on logarithmic scale are adopted and the maximum tolerance of difference between the modified and target spectra is 5 percent.

Table 1 Nonstationary models and equations for simulating artificial accelerograms.

Group	Nonstationary models required	Time-frequency modulating function
Temporal	Intensity envelope	$A(t)$ in Section 2.2

Yu Improved	Intensity envelope and F_p model	$B(t,\omega)$ in Section 2.2 $B_{eq}(t,\omega)$ in Section 2.3

4.2 Non-stationarities of spectrum-compatible ground motions

FIGURE 8 shows the examples of spectrum-compatible accelerograms in each group of two scenarios. Compared with the targets in FIGURE 7a and d, it is obvious the 'Temporal' groups produce accelerograms with stable and over-high frequency content; 'Yu' groups produce acceleration with too lower amplitude for low frequency parts; while, the shapes of the motions in "Improved" are most similar with the targets.

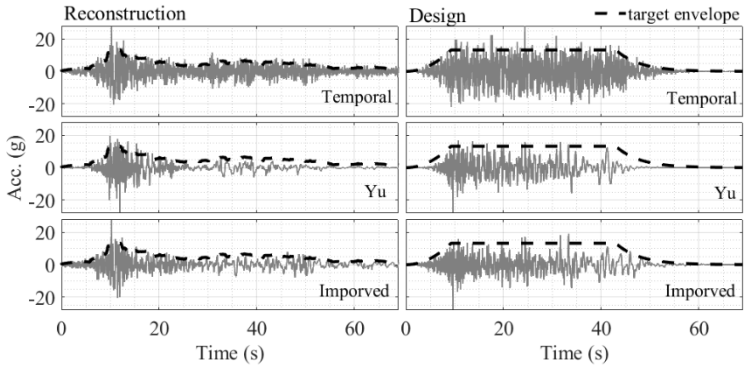

FIGURE 8 Examples of artificial acceleration accelerograms in three groups.

To better show the energy variation of the ground motion in each group, the Husid function [Husid 1969] of all the motions in three groups and two scenarios are evaluated. The Husid function, which is equivalent to the normalized build-up of Arias intensity, can be used to constrain the temporal non-stationarity of acceleration time-history over time duration [Huang and Wang 2017; Colajanni et al. 2020]. For instance, the strong-motion duration can be defined as the time during $0.05 \leq H(t) \leq 0.95$ [Cacciola 2010]. $H(t)$ is the Husid function:

$$H(t) = \frac{\int_0^t y^2(t)\mathrm{d}t}{\int_0^{t_d} y^2(t)\mathrm{d}t} \tag{30}$$

where t_d is the total duration of the ground motion.

FIGURE 9a and b show the mean Husid plots of artificial accelerograms in each group of two scenarios with the targets. It can be seen that the motions in 'Temporal' group (black dot lines) well replicate the target energy accumulation in terms of time. Whereas the 'Yu' group (red dot-dash lines) shows a distinct deviation from the target. In detail, these accelerograms have more energy concentrated at the first half of duration because of the high frequency contents. This situation is well corrected in the 'Improved' group (blue solid lines) as the equivalent average envelope corresponding to the high F_p part is reduced, as shown in FIGURE 3, such that the energy is building up roughly around the target Husid function.

Focusing on the spectral non-stationarities of the ground motion, the mean instantaneous frequencies in each group of two scenarios are calculated and plotted in FIGURE 9c and d with the target curves. To better compare, the F_ps are all smoothed using a 3-second time window. Not Surprisingly, the F_ps in 'Temporal' group remain stable and cannot replicate the time-varying feature. The F_p in 'Yu' group can only fit the targets well within the time interval of strong shaking phase. While the F_ps in 'Improved' groups are very close to the targets.

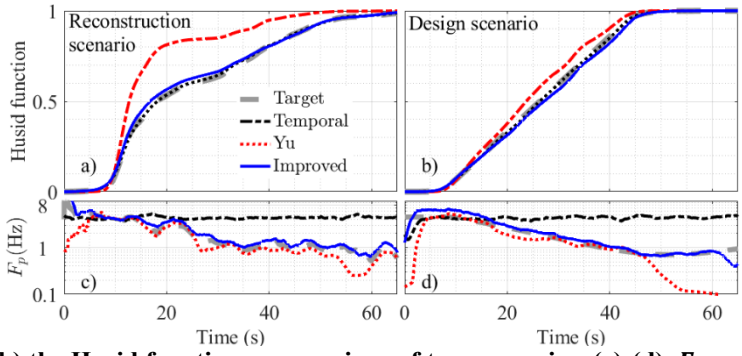

FIGURE 9 (a)-(b) the Husid functions comparison of two scenarios. (c)-(d) F_p comparison of two scenarios.

The above numerical examples show the new method can well replicate both the target temporal and spectral non-stationarities.

5. Sensitivity analysis on site-specific seismic input

In this section, it is demonstrated how the site response affects the acceleration at the surface, i.e., the surface peak ground acceleration ($\mathrm{PGA_{surf}}$) and response spectral acceleration ($\mathrm{SA_{surf}}$), by varying each of the governing factors of the bedrock-motion simulation. We mainly considered two key factors of simulating bedrock motion that may change $\mathrm{PGA_{surf}}$ and $\mathrm{SA_{surf}}$: (i) the time-varying instantaneous frequency and (ii) selecting difference forms of time-frequency modulation function. The objectives are to find whether and to what extent $\mathrm{PGA_{surf}}$ and $\mathrm{SA_{surf}}$ are sensitive to those two factors and to give instructions on how to include non-stationarities of bedrock motion into obtaining site-specific seismic inputs.

Three one-dimension soil profiles with different classification according to Chinese Code GB50011-2010 [2016] are herein considered. The soil profiles in terms of shear wave velocity V_s are plotted in FIGURE 10 (first row); the boreholes B, C and D are sites classified as II, III, and IV respectively based on the V_s and thickness of soft soil according to the code [GB50011-2010 2016]. The modified hyperbolic model (MKZ) [Matasović and Vucetic 1993] is adopted as backbone curve and the non-Masing loading and unloading law revised by Muravskii [2005] to constrain the hysteretic behavior of soil. The parameters for modulus reduction behavior and damping behavior are obtained fitting the analytical curves to measured modulus reduction curve G/G_{max} and damping ratio curve ξ, respectively. The fitting curves are plotted in FIGURE 10 (second row). We use the MATLAB-based code SeismoSoil [Asimaki and Shi 2017] to perform nonlinear site response calculation. As the purpose is to investigate the effects of ground-motion features, neither liquefaction nor pore water pressure generation is considered. The input motions on rock are all considered as outcrop motions in the following studies. Therefore, they are deconvoluted to the bedrock to perform the site propagation.

In section 5.1, we show how we change the two key factors of bedrock-motion simulation in detail. By performing site-response analysis using the same three soil profiles, section 5.2 successively investigates how (i) instantaneous frequency and (ii) selecting difference forms of time-frequency modulation function influence the resultant $\mathrm{PGA_{surf}}$ and $\mathrm{SA_{surf}}$.

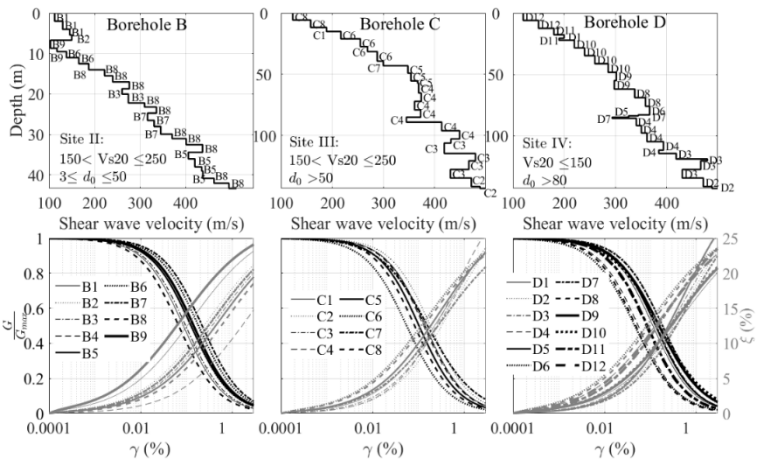

FIGURE 10 V_s profiles (first row) and modulus and damping ratio reduction curves (second row). Each column indicates the same borehole. The site classification is determined by Vs20 and d_0 (covering depth of soil) according to the Chinese code GB 50011-2010 [2016].

5.1 Considered factors for the ground-motion simulation at the bedrock

To investigate the influence of the simulated records on the site response, two sensitivity analyses, based on the 'Improved' group of Reconstruction scenario in Section 4.1 and FIGURE 7, are performed. If not mentioned otherwise, the targets and settings for strong-motion simulation are the same used for simulating the 'Improved' group in the Reconstruction scenario (see Section 4.1). The detail of the two comparisons are:

i. Two target instantaneous-frequency models are considered, i.e. 'Sta-F_p' and 'Decay-F_p', respectively. This allows to investigate the influence of frequency contents. For the model 'Sta-F_p', the target F_p is time-invariant equaling F_{p-sta} where eight levels of F_{p-sta} are used from 1 Hz to 8 Hz. For the scenario 'Decay-F_p', a time-dependent decaying F_p is considered:

$$\log [F_p(t)] = \log(10) - kt \tag{30}$$

where k is the decaying rate of F_p in terms of time on a logarithmic scale and eight levels of k are used as well. To achieve different frequency distribution, power spectra with different peaks are allowed.

ii. Three different time-frequency modulating function models, i.e. 'Temporal', 'Improved', and 'Quasi-real', are also studied to show the effects of modulating function selection. Accelerograms in the group 'Temporal' use the frequency-independent envelope $A(t)$ without considering the frequency variation. The group 'Improved' uses $B_{eq}(t, \omega)$ in Equation (21) proposed in this paper that captures the main feature of the temporal and spectral non-stationarity. Finally, the group 'Quasi-real' uses the normalized time envelopes of the interpolated wavelet spectrum of the record motion at different frequencies to replicate the original ground motion as better as possible. It is worth noting that the 'Temporal' and 'Improved' groups are identical to those presented in Section 4.1.

To study the behavior for the different scenarios under various ground-motion intensity levels, the $\mathrm{PGA_{rock}}$ of the all these simulated bedrock motions are also scaled to three levels, i.e. 0.1g, 0.3g and 0.5g.

5.2 Results and discussion

5.2.1 Frequency contents

FIGURE 11a and b plot the F_p values of the 16 groups of artificial rock motions for the two F_p model scenarios, respectively. Although the fitted F_p functions keep the time-dependent trends and the relative magnitudes between each other defined in the target models, those with extremely high or low values, e.g. 1 Hz and 8 Hz, cannot fit the targets very well. As the EPSD models are finally used to synthesize initial motions, the F_p errors are caused by the

approximate transformation from wavelet model to EPSD model in Equations (10)-(15). Therefore, a power spectral-based central frequency [Régnier et al. 2016] is preferred to represent the concentration of energy in the frequency domain:

$$f_c = \sqrt{\frac{\int_0^\infty f^2 G(f)\mathrm{d}f}{\int_0^\infty G(f)\mathrm{d}f}} \tag{31}$$

where f_c is the central frequency and $G(f)$ is the power spectral of the artificial motion on bedrock. When synthesize the initial motion using Equation (4), the theoretical f_c can be calculated as following [Smith 2003]:

$$f_{c_{theoretical}} = \sqrt{\frac{\int_0^\infty f^2 G_{sum}(f)\mathrm{d}f}{\int_0^\infty G_{sum}(f)\mathrm{d}f}} \tag{32a}$$

$$G_{sum}(f) = \left(\sum_{k=1}^{n}\sqrt{S(\omega_k)\Delta\omega} * \mathrm{conv}(\mathrm{FT}[B(t,\omega_k)], \delta(\omega_k))\right)^2 \tag{34b}$$

in which $\mathrm{conv}(\cdot)$ is the operator of the convolution; $\mathrm{FT}[\cdot]$ is the operator of the Fourier transform, and $\delta(\cdot)$ is the Dirac delta function.

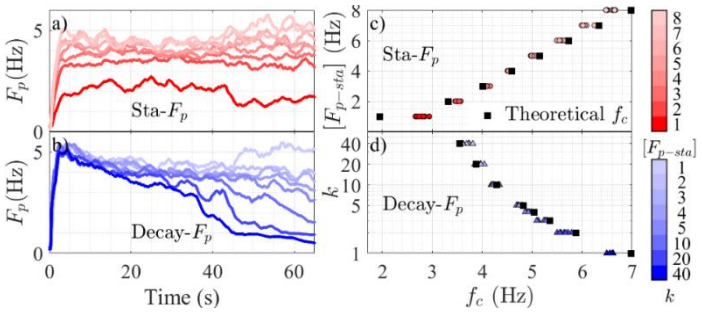

FIGURE 11 (a) $F_p(t)$ of Sta-F_p scenario. (b) $F_p(t)$ of Decay-F_p scenario. (c) Calculated and theoretical central frequency of Sta-F_p scenario. (d) Calculated and theoretical central frequency of Decay-F_p scenario. k denotes the target decaying rate of $F_p(t)$ in term of time on logarithmic scale.

FIGURE 11c and d plot the f_c of the simulated rock motions and their corresponding theoretical values. The results show well agreements between the calculated and theoretical values with the maximum error less than 1Hz, which means the adjustment to fit $\mathrm{SA_{rock}}$ and F_p has limited disturbance on f_c.

The distribution of PGA amplification factors [De Risi et al. 2019] as a function of f_c with different shaking intensities and site conditions are plotted in FIGURE 12a. Regardless of the $\mathrm{PGA_{rock}}$ level and site condition, similar second-order polynomial relationships between the mean $\mathrm{PGA_{surf}}$ and mean f_c can be fitted (FIGURE 12a). $\mathrm{PGA_{surf}}$ has a trend first increasing and then decreasing as the f_c increases. The levels of change in terms of f_c decrease with higher shaking intensity and softer site condition, which is caused by the suppression of high-frequency content because of stronger nonlinearity and lower resonance frequency. However, it must be noted that the variation of mean $\mathrm{PGA_{surf}}$ with respect to f_c is not distinct, which is close to or even smaller than its inter-group variation.
FIGURE 12b plots the $\mathrm{SA_{surf}}$ in terms of f_c with different shaking intensities and site conditions. Although the $\mathrm{SA_{surf}}$ with different f_c and $\mathrm{PGA_{rock}} = 0.1\mathrm{g}$ at three boreholes are almost the same, the results in the second and third row highlight the more distinct difference with low and moderate natural periods and stronger $\mathrm{PGA_{rock}}$ from 0.3 g to 0.5 g. In Scenario 'Sta-F_p', $\mathrm{SA_{surf}}$ with $T \leq 0.5$ s, especially with $0.1\,\mathrm{s} \leq T \leq 0.5\,\mathrm{s}$, significantly increases and $\mathrm{SA_{surf}}$ with $0.5\,\mathrm{s} \leq T \leq 1\,\mathrm{s}$ slightly decreases as the f_c increases. Whereas in Scenario 'Decay-F_p', the trend is same, but the change is much slighter.

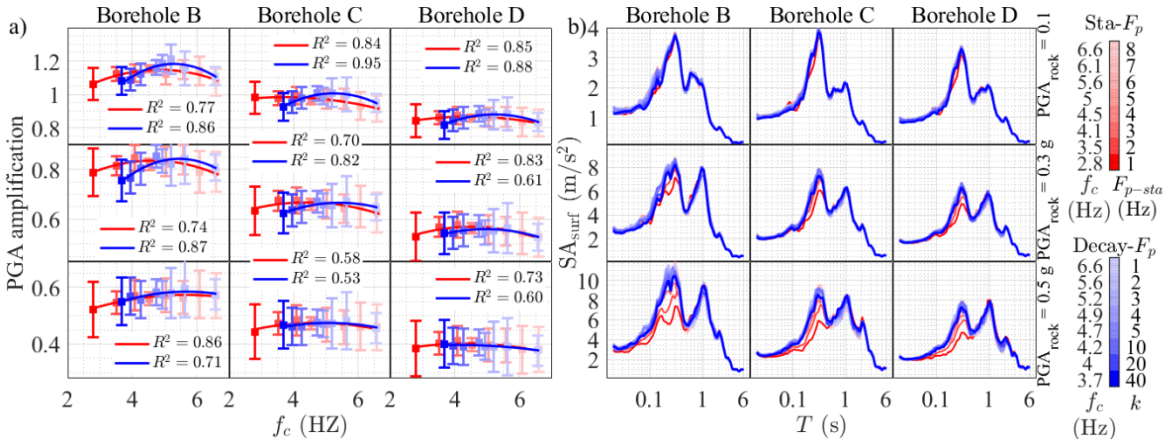

FIGURE 12 (a) PGA amplification with their uncertainties (error bars, mean±std) and fits of mean (lines) in Scenario 'Sta-F_p' (Red) and 'Decay-F_p' (Blue). (b) Spectral acceleration on surface of Scenario 'Sta-F_p' (Red solid lines) and 'Decay-F_p' (Blue dash lines). In (a) and (b), Each column denotes results on the same site and each row the same $\mathrm{PGA_{rock}}$ level. F_{p-sta} is the target stable F_p in Sta-F_p scenario and k denotes the target decaying rate of $F_p(t)$ in terms of time on logarithmic scale in Decay-F_p scenario. R^2 denotes the Coefficient of determination of least-square fit.

Detailed examination indicates that the reason for such observation is mainly due to the difference of energy in different frequency bands and the change of frequency contents in terms of time, other than the change of nonlinear soil properties. The mean nonlinear transfer functions of soil profiles for $\mathrm{PGA_{rock}} = 0.5\ \mathrm{g}$ are plotted in FIGURE 13a. Slightly difference with $f \geq 1$ Hz is observed between two scenarios. However, the difference is so small (less than 20%), and the inter-scenario nonlinear transfer functions are very close. Thus, those cannot be the attribution of the above-mentioned massive difference in $\mathrm{SA_{surf}}$.

FIGURE 13b also shows examples of mean smoothed Fourier amplitude spectra of artificial accelerograms in three groups. They respectively correspond to the two groups in Scenario 'Sta-F_p' with very different f_c, i.e. A1 (f_c=3.5Hz) and A2 ($f_c = 6.6$ Hz), and one group in Scenario 'Decay-F_p' having close f_c with A1, i.e. B1 (f_c=3.7Hz). On one hand, we can notice that the Fourier spectra of A1 are distinctly larger than A2 with $f > \sim 2$ Hz and smaller than A2 with $f < \sim 2$ Hz. When the shaking is intensive, e.g. $\mathrm{PGA_{rock}} = 0.5\ \mathrm{g}$, the strong nonlinearity of soil profiles suppresses the high frequency of the input motion, making the spectral difference between A1 and A2 more distinct. On the other hand, the comparison between A1 and B1 illustrates the location of high frequency is equally important. A1 and B1 have similar shape and amplitude of spectra, thus having similar f_c. Moreover, the Fourier spectra of B1 with $f > \sim 2$Hz is even smaller than A1. However, the high-frequency part of B1 occurs at the initial of the accelerogram where the intensity is not so strong to trigger high nonlinearity, causing the $\mathrm{SA_{surf}}$ of B1 with $T \leq 0.5$ s much larger than A1.

The discussion above concludes that for low $\mathrm{PGA_{rock}}$ (0.1 g), the change of frequency content of spectral-compatible motion at bedrock only slightly influences the $\mathrm{PGA_{surf}}$, which is not essentially very significant. While for moderate and large $\mathrm{PGA_{rock}}$ (0.3g and 0.5g), $\mathrm{SA_{surf}}$ is influenced by the concentration of energy in terms of frequency and the time location of high-frequency contents. Therefore, the frequency contents of the input motion should be carefully examined that not only the power spectrum should match the empirical estimation, but also the time-varying feature of frequency contents should be determined carefully to avoid underestimation of the surface seismic input.

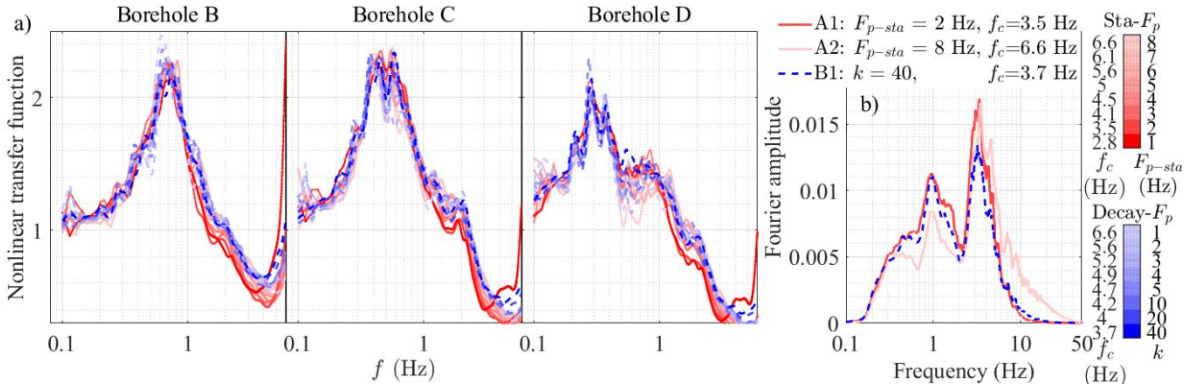

FIGURE 13 (a) Nonlinear transfer functions of Scenario 'Sta-F_p' (Red solid lines) and 'Decay-F_p' (Blue dash lines) with $\mathrm{PGA_{rock}} = 0.5$ g. (b) Examples of Fourier amplitude of artificial accelerogram on rock outcrop. F_{p-sta} is the target stable F_p in Sta-F_p scenario and k denotes the target decaying rate of $F_p(t)$ in terms of time on logarithmic scale in Decay-F_p scenario.

5.2.2 time-frequency modulating function model

FIGURE 14 shows examples of time-frequency modulating functions in each group. 'Temporal' group have the same modulating functions at different frequencies. The shape of modulating functions of group 'Quasi-real' is similar with group 'Improved', while are much finer with high frequencies and coarser with low frequencies resulted from the nature of the resolution of the wavelet transform. The results indicate the modulating function of 'Quasi-real' most closely represents the detailed character of the record.

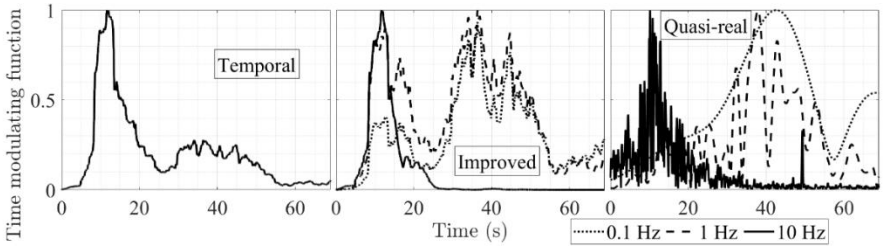

FIGURE 14 Examples of time-modulating functions at different frequencies. Three lines in 'Temporal' panel overlap with each other.

FIGURE 15a and FIGURE 15b plot respectively the PGA amplification and the $\mathrm{SA_{surf}}$ between the artificial rock motions and the record at the surface of the three soil profiles. On one hand, it can be seen that, for low-intensity level with $\mathrm{PGA_{rock}} = 0.1$ g, the 'Temporal' groups produce close results of $\mathrm{SA_{surf}}$ with long periods but overestimate the $\mathrm{PGA_{surf}}$ and $\mathrm{SA_{surf}}$ with short periods when the site is hard; for moderate and high-intensity level, the 'Temporal' groups underestimate the $\mathrm{SA_{surf}}$ with moderate periods. It illustrates the significance of considering frequency variation same with Section 5.2.1. On the other hand, regardless the intensity levels and site conditions, although the 'Improve' time-modulating function uses the approximate $L(t,f)$ in Equation (6) with details of frequency distribution lost (FIGURE 14b), it produces as good results as the finer time-modulating function of 'Quasi-real' group, both very close to the record.

Overall, for both small and large $\mathrm{PGA_{rock}}$ level, it is all recommended to use the new, improved time-modulating function to simulate ground motions on bedrock.

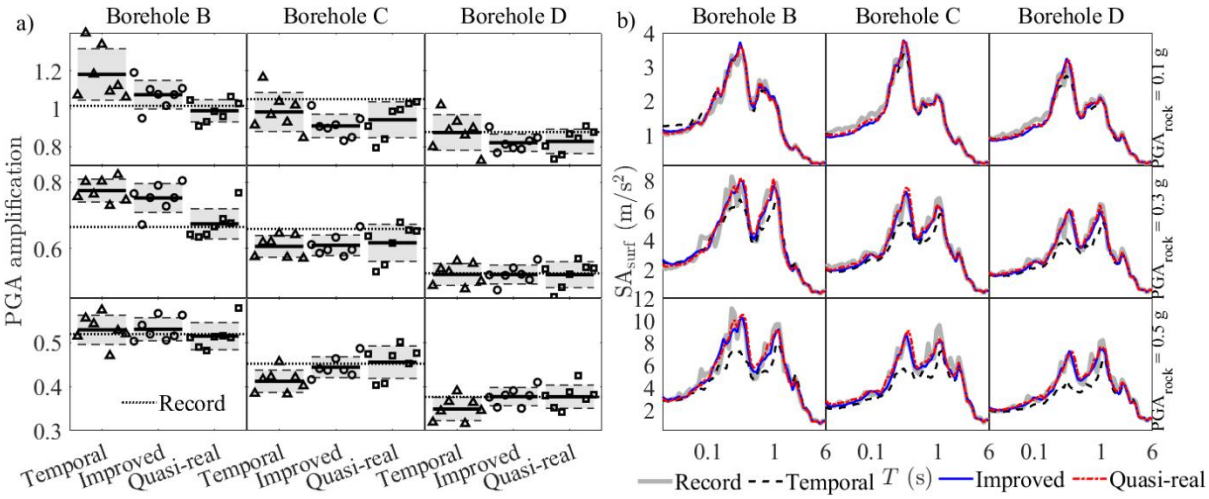

FIGURE 15 (a) Surface PGA difference from the record with different time-modulating functions. Triangles, circles, and rectangles indicate 'Temporal', 'Improved', and 'Quasi-real' scenarios, respectively. Black solid lines denote mean and dash lines denote mean±std. (b) Surface SA with different time-modulating functions. Each column denotes results on the same site and each row the same PGA_{rock} level.

6. Conclusion

In this study, we first proposed a time-frequency modulating function of ground motion with desired temporal and spectral non-stationarities, and then developed a simulation method for ground motion matching of multiple targets. Based on these, we performed extent studies on simulating accelerograms on bedrock. The conclusions obtained in this study are as follows:

1) The new time-frequency modulating function replaces the time-envelope function of accelerogram with the new equivalent average-envelope function of EPSD and has more close energy build-up with the target. Moreover, the model not only can simulate the nonstationary characteristics of ground motion very well but also has statistical modal parameters classified according to magnitude and distance, which is very suitable for engineering application.

2) The new period-by-period simulation method based on proposed stochastic model can not only match multiple targets, such as the PGA and the spectrum, but can also well replicate both the desired temporal and spectral non-stationarities with simple uncoupled intensity and instantaneous frequency models and parameters, which is efficient and easy to use in engineering practice.

3) If not considering liquefaction, the frequency content of the ground-motion, including the energy concentration in terms of frequency and decaying with respect to time, have a great impact on the site response with moderate and large PGA level (0.3g and 0.5g), thereby requiring careful determination when simulating ground motion on bedrock .

4) Using the F_p-related time-modulating function to approximate the real ground motion brings close enough results with the record for nonlinear site response regardless PGA level and site condition, thus is recommended to simulate ground motion on bedrock in engineering practice.

The developed work in this paper, including a new proposed fully nonstationary model, a ground-motion simulation method and instructions on how to consider non-stationarities for bedrock-motion simulation, is applicable to produce more realistic site-specific seismic input on soil sites.

ACKNOWLEDGEMENTS

The financial supports from the National Natural Science Foundation of China (No. 51878627 and No. 51478440) are much appreciated. S.W. gratefully acknowledges the China Scholarship Council for supporting a 1-year research visit

to the School of Earth Sciences at the University of Bristol.

Reference

Amin M, Ang AHS. Nonstationary stochastic models of earthquake motions. Journal of the Engineering Mechanics 1968; 94(2): 559–584.

Asimaki D, Shi J. SeismoSoil User Manual,v.1.3. 2017 1–35.

Assimaki D, Ledezma C, Montalva GA, et al. Site effects and damage patterns. Earthquake Spectra 2012; 28(SUPPL.1): 55–74. doi: 10.1193/1.4000029.

Assimaki D, Li W. Site- and ground motion-dependent nonlinear effects in seismological model predictions. Soil Dynamics and Earthquake Engineering 2012; 32(1): 143–151. doi: 10.1016/j.soildyn.2011.06.013.

Assimaki D, Li W, Steidl J, et al. Quantifying nonlinearity susceptibility via site-response modeling uncertainty at three sites in the Los Angeles basin. Bulletin of the Seismological Society of America 2008; 98(5): 2364–2390. doi: 10.1785/0120080031.

Al Atik L, Abrahamson N. An Improved method for nonstationary spectral matching. Earthquake Spectra 2010; 26(3): 601–617. doi: 10.1193/1.3459159.

Baker JW. Conditional mean spectrum: Tool for ground-motion selection. Journal of Structural Engineering 2011; 137(3): 322–331. doi: 10.1061/(ASCE)ST.1943-541X.0000215.

Beck JL, Papadimitriou C. Moving resonance in nonlinear response to fully nonstationary stochastic ground motion. Probabilistic Engineering Mechanics 1993; 8(3–4): 157–167. doi: 10.1016/0266-8920(93)90011-J.

BSSC. NEHRP Recommended seismic provisions for new buildings and other structures, FEMA P-1050. 2015.

Cacciola P. A stochastic approach for generating spectrum compatible fully nonstationary earthquakes. Computers & Structures 2010; 88(15–16): 889–901. doi: 10.1016/j.compstruc.2010.04.009.

Cacciola P, Zentner I. Generation of response-spectrum-compatible artificial earthquake accelerograms with random joint time–frequency distributions. Probabilistic Engineering Mechanics 2012; 28: 52–58. doi: 10.1016/j.probengmech.2011.08.004.

Cakir T. Evaluation of the effect of earthquake frequency content on seismic behavior of cantilever retaining wall including soil–structure interaction. Soil Dynamics and Earthquake Engineering 2013; 45: 96–111. doi: 10.1016/j.soildyn.2012.11.008.

CEN. Eurocode 8: design of structures for earthquake resistance. Part 1: General rules, seismic actions and rules for buildings. 2005; 240.

Chiou B, Darragh R, Gregor N, et al. NGA project strong-motion database. Earthquake Spectra 2008; 24(1): 23–44. doi: 10.1193/1.2894831.

Chopra AK. DYNAMICS OF STRUCTURES theory and applications to earthquake engineering. Cambridge University Press, Cambridge, 2012.

Colajanni P, Pagnotta S, Testa G. Comparison of fully non-stationary artificial accelerogram generation methods in reproducing seismicity at a given site. Soil Dynamics and Earthquake Engineering 2020; 133: 106-135. doi: 10.1016/j.soildyn.2020.106135.

Conte JP, Peng BF. Fully nonstationary analytical earthquake ground-motion model. Journal of Engineering Mechanics 1997; 123(1): 15–24. doi: 10.1061/(ASCE)0733-9399(1997)123:1(15).

GB50011-2010. Code for seismic design of buildings, version 2016 National Standard of the People's Republic of China. China Building Industry Press, Beijing, 2016.

Giaralis A, Spanos PD. Wavelet-based response spectrum compatible synthesis of accelerograms—Eurocode application (EC8). Soil Dynamics and Earthquake Engineering 2009; 29(1): 219–235. doi:

10.1016/j.soildyn.2007.12.002.

Hancock J, Watson-Lamprey J, Abrahamson NA, et al. An improved method of matching response spectra of recorded earthquake ground motion using wavelets. Journal of Earthquake Engineering 2006; 10(sup001): 67–89. doi: 10.1080/13632460609350629.

Heredia-Zavoni E. The complete SRSS modal combination rule. Earthquake Engineering & Structural Dynamics 2011; 40(11): 1181–1196. doi: 10.1002/eqe.1082.

Huang DR, Wang G. Energy-compatible and spectrum-compatible (ECSC) ground motion simulation using wavelet packets. Earthquake Engineering & Structural Dynamics 2017; 46(11): 1855–1873. doi: 10.1002/eqe.2887.

Husid R. Caracteristicas de terremotos—analisis general. Revista del IDEM 1969; 8: 21–42.

Iervolino I, Galasso C, Cosenza E. REXEL: Computer aided record selection for code-based seismic structural analysis. Bulletin of Earthquake Engineering 2010; 8(2): 339–362. doi: 10.1007/s10518-009-9146-1.

Iervolino I, De Luca F, Cosenza E. Spectral shape-based assessment of SDOF nonlinear response to real, adjusted and artificial accelerograms. Engineering Structures 2010; 32(9): 2776–2792. doi: 10.1016/j.engstruct.2010.04.047.

Iyama J, Kuwamura H. Application of wavelets to analysis and simulation of earthquake motions. Earthquake Engineering & Structural Dynamics 1999; 28(3): 255–272. doi: 10.1002/(SICI)1096-9845(199903)28:3<255::AID-EQE815>3.0.CO;2-C.

Iyengar RN, Iyengar KTSR. A nonstationary random process model for earthquake accelerograms. Bulletin of the Seismological Society of America 1969; 59(3): 1163–1188.

Kaul MK. Stochastic characterization of earthquakes through their response spectrum. Earthquake Engineering & Structural Dynamics 1978; 6(5): 497–509. doi: 10.1002/eqe.4290060506.

Kelkar SS, Grigsby LL, Langsner J. An Extension of Parseval's Theorem and its use in calculating transient energy in the frequency domain. IEEE Transactions on Industrial Electronics 1983; IE-30(1): 42–45. doi: 10.1109/TIE.1983.356702.

Kianoush MR, Ghaemmaghami AR. The effect of earthquake frequency content on the seismic behavior of concrete rectangular liquid tanks using the finite element method incorporating soil–structure interaction. Engineering Structures 2011; 33(7): 2186–2200. doi: 10.1016/j.engstruct.2011.03.009.

Lee TH, Mosalam KM. Probabilistic seismic evaluation of reinforced concrete structural components and systems. Berkeley, 2006.

Lilhanand K, Tseng WS. Development and application of realistic earthquake time histories compatible with multiple damping response spectra. in *Proceedings of Ninth World Conference on Earthquake Engineering* 1988 819–824.

Lilhanand K, Tseng W. Generation of synthetic time histories compatible with multiple-damping design response spectra. Netherlands: Balkema. in *Transactions of the 9th international conference on structural mechanics in reactor technology* 1987.

Matasović N, Vucetic M. Cyclic characterization of liquefiable sands. J. Geotech. Geoenviron. Eng. 1993; 119(11): 1805–1822.

Muravskii G. On description of hysteretic behaviour of materials. International Journal of Solids and Structures 2005; 42(9–10): 2625–2644. doi: 10.1016/j.ijsolstr.2004.10.009.

Nigam NC, Mark WD. Introduction to random vibrations by N. C. Nigam. The Journal of the Acoustical Society of America 1984; 76(6): 1871–1871. doi: 10.1121/1.391500.

Preumont A. The generation of non-separable artificial earthquake accelerograms for the design of nuclear power plants. Nuclear Engineering and Design 1985; 88(1): 59–67. doi: 10.1016/0029-5493(85)90045-7.

Priestley MB. Spectral analysis and time series: probability and mathematical statistics. Academic Press: New York, 1987.

Radu A, Grigoriu M. A Site-specific ground-motion simulation model: Application for Vrancea earthquakes. Soil Dynamics and Earthquake Engineering 2018; 111(February): 77–86. doi: 10.1016/j.soildyn.2018.04.025.

Régnier J, Bonilla LF, Bard PY, et al. International benchmark on numerical simulations for 1D, nonlinear site response (Prenolin): Verification phase based on canonical cases. Bulletin of the Seismological Society of America 2016; 106(5): 2112–2135. doi: 10.1785/0120150284.

Régnier J, Cadet H, Bard P. Empirical quantification of the impact of nonlinear soil behavior on site response. Bulletin of the Seismological Society of America 2016; 106(4): 1710–1719. doi: 10.1785/0120150199.

Rezaeian S, Der Kiureghian A. A stochastic ground motion model with separable temporal and spectral nonstationarities. Earthquake Engineering & Structural Dynamics 2008; 37(13): 1565–1584. doi: 10.1002/eqe.831.

De Risi R, Penna A, Simonelli AL. Seismic risk at urban scale: the role of site response analysis. Soil Dynamics and Earthquake Engineering 2019; 123(April): 320–336. doi: 10.1016/j.soildyn.2019.04.011.

Sextos A, De Risi R, Pagliaroli A, et al. Local site effects and incremental damage of buildings during the 2016 central Italy earthquake sequence. Earthquake Spectra 2018; 34(4): 1639–1669. doi: 10.1193/100317EQS194M.

Shinozuka M, Jan C-M. Digital simulation of random processes and its applications. Journal of Sound and Vibration 1972; 25(1): 111–128. doi: 10.1016/0022-460X(72)90600-1.

Smith SW. Fourier transform properties. in *Digital Signal Processing* Elsevier, 2003 185–208.

Spanos PD, Failla G. Evolutionary spectra estimation using wavelets. Journal of Engineering Mechanics 2004; 130(8): 952–960. doi: 10.1061/(ASCE)0733-9399(2004)130:8(952).

Todorovska M. Estimation of instantaneous frequency of signals using the continuous wavelet transform. Los Angeles, California, 2001.

Tsioulou A, Taflanidis AA, Galasso C. Hazard-compatible modification of stochastic ground motion models. Earthquake Engineering & Structural Dynamics 2018a; 47(8): 1774–1798. doi: 10.1002/eqe.3044.

Tsioulou A, Taflanidis AA, Galasso C. Modification of stochastic ground motion models for matching target intensity measures. Earthquake Engineering & Structural Dynamics 2018b; 47(1): 3–24. doi: 10.1002/eqe.2933.

Tsioulou A, Taflanidis AA, Galasso C. Validation of stochastic ground motion model modification by comparison to seismic demand of recorded ground motions. Bulletin of Earthquake Engineering 2019; 17(6): 2871–2898. doi: 10.1007/s10518-019-00571-x.

Wang D, Fan ZL, Hao SW, et al. An evolutionary power spectrum model of fully nonstationary seismic ground motion. Soil Dynamics and Earthquake Engineering 2018; 105(March 2017): 1–10. doi: 10.1016/j.soildyn.2017.11.014.

Wang SQ, Yu RF, Li XJ, et al. Simulation method of ground motion matching for multiple targets and effects of fitting parameter variation on the distribution of PGD. Earthquake and Structures 2019; 16(5): 563–573. doi: https://doi.org/10.12989/eas.2019.16.5.563.

Wilson EL, Der Kiureghian A, Bayo EP. A replacement for the srss method in seismic analysis. Earthquake Engineering & Structural Dynamics 1981; 9(2): 187–192. doi: 10.1002/eqe.4290090207.

Yamamoto Y, Baker JW. Stochastic model for earthquake ground motion using wavelet packets. Bulletin of the Seismological Society of America 2013; 103(6): 3044–3056. doi: 10.1785/0120120312.

Yang DX, Zhou JL. A stochastic model and synthesis for near-fault impulsive ground motions. Earthquake Engineering & Structural Dynamics 2015; 44(2): 243–264. doi: 10.1002/eqe.2468.

Yazdani Y, Alembagheri M. Nonlinear seismic response of a gravity dam under near-fault ground motions and equivalent pulses. Soil Dynamics and Earthquake Engineering 2017; 92(June 2016): 621–632. doi: 10.1016/j.soildyn.2016.11.003.

Yu YX, Li SY, Xiao L. Development of ground motion attenuation relations for the new seismic hazard map of China. Earthq. Disaster Prev 2013; 8(1): 24–33.

Yu RF, Yuan MQ, Yu YX. Developed empirical model for simulation of time-varying frequency in earthquake ground motion. Earthquakes and Structures 2015; 8(6): 1463–1480. doi: 10.12989/eas.2015.8.6.1463.

Yu RF, Zhou XY. Simplifications of CQC method and CCQC method. Earthquake Engineering and Engineering Vibration 2007; 6(1): 65–76. doi: 10.1007/s11803-007-0640-7.

Zhou XY, Yu RF, Dong D. Complex mode superposition algorithm for seismic responses of non-classically damped linear MDOF system. Journal of Earthquake Engineering 2004; 8(4): 597–641.